

Determining the 3P_0 excited-state tune-out wavelength of ^{174}Yb in a triple-magic lattice

Tim O. Höhn,^{1,2} René A. Villela,^{1,2} Er Zu,^{1,2} Leonardo Bezzo,^{1,2} Ronen M. Kroeze,^{1,2} and Monika Aidelsburger^{1,2,3,*}

¹Fakultät für Physik, Ludwig-Maximilians-Universität, 80799 München, Germany

²Munich Center for Quantum Science and Technology (MCQST), 80799 München, Germany

³Max-Planck-Institut für Quantenoptik, 85748 Garching, Germany

(Dated: December 19, 2024)

Precise state-dependent control of optical potentials is of great importance for various applications utilizing cold neutral atoms. In particular, tune-out wavelengths for the clock state pair in alkaline-earth(-like) atoms provide maximally state-selective trap conditions that hold promise for the realization of novel approaches in quantum computation and simulation. While several ground-state tune-out wavelengths have been determined, similar experimental studies for metastable excited states are challenged by inelastic collisions and Raman losses, so far prohibiting precise measurements of excited-state tune-out conditions. In this work we report on the measurement of a tune-out wavelength for the metastable 3P_0 clock state in ^{174}Yb at 519.920(9) THz. In order to circumvent collisional losses, we isolate individual 3P_0 atoms in a clock-magic-wavelength lattice at 759 nm. To minimize the limitation imposed by Raman scattering, we further implement resolved sideband cooling on the clock transition, which allows us to reduce the lattice depth and surpass lifetimes of 5 s. The precision of the tune-out measurement is further enhanced by fluorescence imaging in a triple-magic configuration, where we implement molasses cooling on the 3P_1 intercombination line and identify a magic angle of $38.5(9)^\circ$ in the clock-magic lattice.

I. INTRODUCTION

Alkaline-earth(-like) (AEL) atoms have been utilized for a plethora of remarkable applications, from advanced quantum computation protocols [1–4] to quantum simulation of the $SU(N)$ Fermi-Hubbard model [5–8]. In particular the ultra-narrow transition to the 3P_0 state has enabled the development of extremely accurate optical lattice clocks [9–11], the realization of highly entangled states for enhanced metrology [12], as well as the realization of spin-orbit coupling [13] and artificial gauge fields in synthetic dimensions [14, 15]. A crucial ingredient for these results is the precise cancellation of differential Stark shifts in magic traps [16].

However, for certain applications like site-resolved addressing [1, 17, 18] or the simulation of mass-imbalanced particles [19] and lattice gauge theories [20], state-selective traps constitute an invaluable resource. The extreme case of a fully vanishing atom-light coupling of one state at a tune-out wavelength, while the other state retains a finite polarizability, has been employed for erasure conversion of quantum gate errors [4], and it has been suggested to be used for simulations of twisted bilayer systems [21, 22], the realization of novel quantum gates [23], and the separation into storage and transport traps for quantum processors [24, 25]. Since this condition requires equal blue- and red-detuned polarizability contributions from the dominant transitions, tune-out wavelengths in alkali atoms only exist close to transitions, resulting in detrimental near-resonant scattering. For AEL atoms, the strongly decoupled transition manifolds for the ground and metastable excited state in turn result in far-detuned tune-out wavelengths and thus provide the ability to perform high-fidelity resorting operations or local lightshift applications with minimal scattering.

Furthermore, as precise *ab initio* polarizability calculations for the $^1S_0 - ^3P_0$ clock state pair are highly nontrivial, measurements of distinct points such as tune-out wavelengths are crucial to test and improve the accuracy of these models [28]. In this work we demonstrate the versatility of shaping the polarizabilities of various states by measuring the magic angle for the narrow $^1S_0 \rightarrow ^3P_1$ cooling transition in ^{174}Yb , allowing for a triple-magic condition in the clock-magic lattice at 759 nm, and determining the tune-out wavelength for the 3P_0 clock state, where its polarizability exhibits a zero crossing.

Compared to the ground-state tune-out measurements performed in AEL atoms so far, which have been based on parametric heating schemes with long-lived ground-state atoms trapped in one dimensional (1D) lattices [26, 29], the detection of a tune-out wavelength for the metastable 3P_0 state is significantly challenged by several factors. First, strong inelastic collisions of nearby 3P_0 atoms result in fast losses [30, 31], limiting Kapitza-Dirac scattering measurements using pulsed optical lattices with a Bose-Einstein condensate (BEC) [32–36]. Second, deep optical traps induce strong off-resonant Raman scattering [27, 37], such that one has to resort to shallow optical lattices to reach the sufficiently long lifetimes necessary for parametric heating measurements, as used in this work [26, 29]. To this end, we combine ground-state cooling of bosonic ^{174}Yb atoms on the clock transition in a 2D lattice [38] with a high signal-to-noise ratio detection scheme using magic-angle molasses cooling during fluorescence imaging, where the former allows for a sufficient isolation of individual atoms and suppresses tunneling, while the latter provides the resolution to detect even smallest lifetime changes.

II. EXPERIMENTAL RESULTS

The experiment starts by directly loading $\simeq 70 \times 10^3$ ^{174}Yb atoms from a magneto-optical trap (MOT) into a $\simeq 140 \mu\text{K}$ deep clock-magic optical lattice at $\lambda = 759.3$ nm. Compared

* Monika.Aidelsburger@physik.uni-muenchen.de

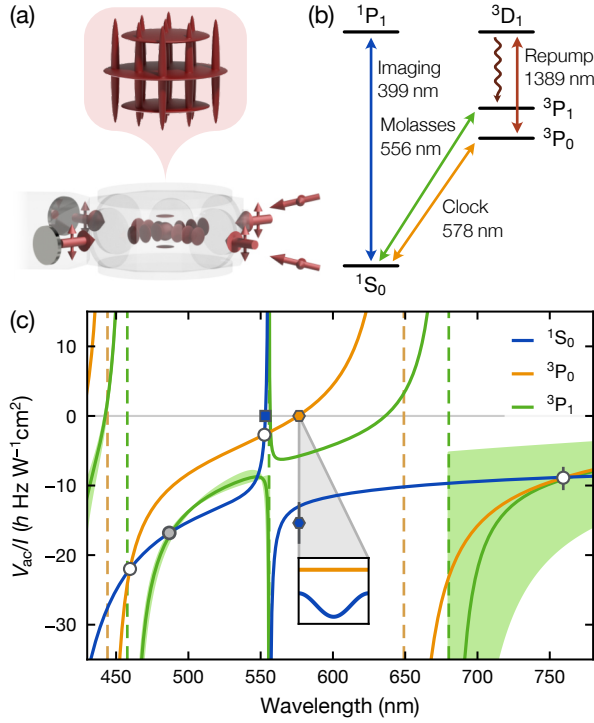


FIG. 1. Experimental setup, simplified level structure, and ac polarizabilities of ^{174}Yb . (a) Sketch of the 3D clock-magic lattice. Double-sided arrows indicate the polarization of the individual lattice beams. (b) Simplified level structure including the clock ($^1\text{S}_0 \rightarrow ^3\text{P}_0$), repumping ($^3\text{P}_0 \rightarrow ^3\text{D}_1$), imaging ($^1\text{S}_0 \rightarrow ^1\text{P}_1$) and molasses cooling transition ($^1\text{S}_0 \rightarrow ^3\text{P}_1$). (c) Light shifts of the three lowest-lying states in linearly polarized traps, using an empirical model [26, 27]. The green shaded area highlights the tunability of the total $^3\text{P}_1(m_J = 0)$ light shift by adjusting the angle of the quantization axis. Round markers indicate the measured magic wavelengths ($^1\text{S}_0 \rightarrow ^3\text{P}_0$ white, $^1\text{S}_0 \rightarrow ^3\text{P}_1$ gray), hexagonal markers the $^3\text{P}_0$ tune-out wavelength (orange, corresponding measured $^1\text{S}_0$ polarizability in blue) and the square marker depicts the $^1\text{S}_0$ tune-out wavelength. Inset: Schematic trapping potential at the $^3\text{P}_0$ tune-out wavelength.

to our previous work, our setup has been upgraded to a 3D lattice, which is used for loading and imaging of the atoms [26]. The 3D geometry consists of two orthogonal, retro-reflected and vertically polarized horizontal lattices and a shallow-angle vertical lattice as illustrated in Fig. 1(a). The 3D lattice allows us to reach total potential depths of $\approx 450 \mu\text{K}$ and strong confinement in all directions. Fluorescence imaging is realized by implementing molasses cooling on the $^1\text{S}_0 \rightarrow ^3\text{P}_1$ intercombination line [Fig. 1(b)] [1, 39–41]. Since this transition is only 183 kHz wide, high-fidelity imaging relies on magic trapping [41–43]. This condition is generally not fulfilled in a clock-magic optical lattice. The finite total electronic angular momentum of the $^3\text{P}_1$ state, however, induces a significant tensor shift, which can be leveraged to achieve a triple-magic condition [Fig. 1(c)], as has been demonstrated for ^{171}Yb [1]. Here, one can utilize the dependence of the tensor shift on the relative angle θ between the trap polarization and the quantization axis. In the case of ^{174}Yb , the total expected resonance shift for the Zeeman substate m_J , in the presence of a magnetic

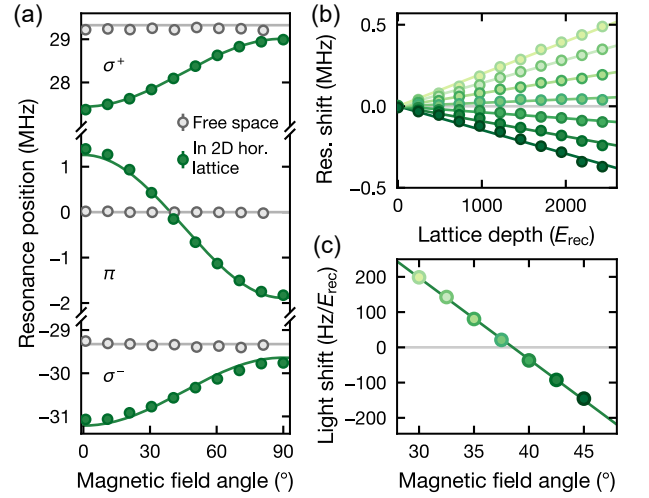


FIG. 2. Measuring the magic angle for the $^1\text{S}_0 \rightarrow ^3\text{P}_1$ transition at 759 nm. (a) Light shifted $^1\text{S}_0 \rightarrow ^3\text{P}_1$ σ^+ , π , and σ^- transitions (green) for various magnetic field angles relative to the vertical lattice polarization, and stationary free-space resonances (gray). The solid lines correspond to a single fit to the data using Eq. (1). The error bars are obtained from the Lorentzian resonance fit uncertainty and are smaller than the datapoints. (b) Resonance shifts of the π transition for various magnetic field angles [color code as in (c)] and lattice depths close to the magic angle. The data is fitted with a linear function (solid lines). (c) The fitted slopes are used to determine the magic angle using a linear fit since the curvature of the light shift in this regime is negligible.

field B can be expressed as

$$\Delta V_{\text{ac}} = -\frac{I}{2c\epsilon_0} \left(\Delta\alpha_s + \alpha_t \frac{3\cos^2\theta - 1}{2} (3m_J^2 - 2) \right) + \mu B m_J, \quad (1)$$

where $\Delta\alpha_s$ is the scalar differential polarizability, α_t is the tensor polarizability of the $^3\text{P}_1$ state, $\mu = g_J \mu_B$ is the magnetic moment, and μ_B is the Bohr magneton.

To ascertain the magic angle in ^{174}Yb , we perform atom loss spectroscopy on all three m_J transitions in a $\approx 240 \mu\text{K} \approx 2400 E_{\text{rec}}$ deep 2D lattice, where $E_{\text{rec}} = h^2/(2m\lambda^2)$ is the lattice recoil energy with h being Planck's constant, and m the atomic mass. This spectroscopy is performed for various magnetic field angles relative to the vertical polarization axis at a total field of $B \approx 14 \text{ G}$ and we compare the resulting resonance positions to the case of free-space resonances to determine the light shift according to Eq. (1) [Fig. 2(a)]. The latter are determined within a short time-of-flight period during which the lattice is quenched off, while the direction and intensity of the circularly polarized spectroscopy beam is chosen such that the projection on the individual transitions is sufficiently large over the whole angle range and yields only minimally power-broadened linewidths, which we find to be the case for a beam approximately co-propagating with one of the horizontal lattice arms and $I \approx I_{\text{sat}}$. This yields a magic angle for the $m_J = 0$ state at $\approx 35^\circ$ and further demonstrates the existence of a near-magic condition for the transitions to the $m_J = \pm 1$ states for magnetic fields orthogonal to the lattice polarization.

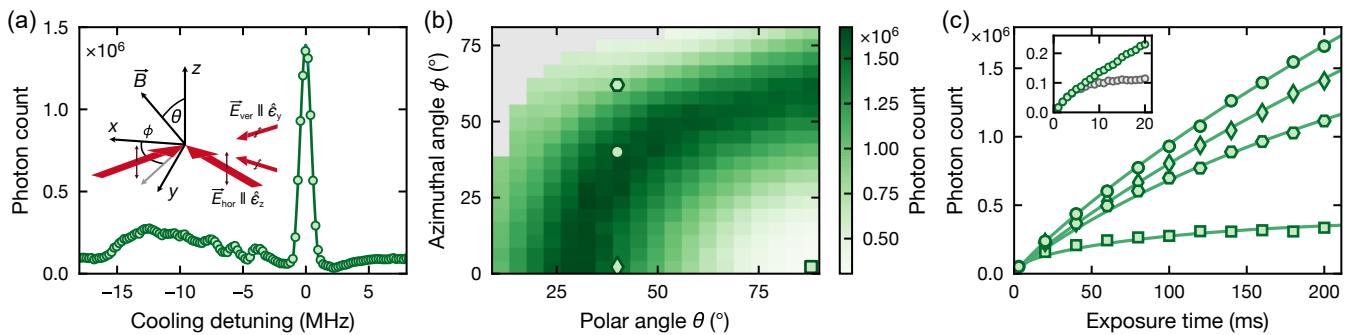


FIG. 3. **Molasses cooling in a 3D lattice.** (a) For a quasi-magic condition in a $\simeq 400 \mu\text{K}$ deep 3D lattice we observe a $\simeq 600 \text{ kHz}$ wide molasses resonance close to the free-space $^3\text{P}_1 \pi$ transition leading to a strongly enhanced collection of fluorescence photons after 200 ms exposure time with weak 399 nm probe light. In contrast, the light-shifted σ^\pm transitions do not allow for efficient cooling of the whole cloud. The solid line is a Lorentzian fit to the cooling resonance data. Inset: Lattice beams (bright red single arrows), corresponding polarization vectors (dark red double-sided arrows), and magnetic field configuration. (b) Cooling efficiency for different magnetic field orientations. While it is not possible to simultaneously reach the magic angle for the horizontal and vertical lattices, the resonance linewidth enables sufficiently quasi-magic conditions for a broad range of B -field angles. (c) Evolution of the photon counts for varied exposure times. The only slightly curved trend observed for various magnetic field directions [indicated by the markers in (b)], demonstrates that the heating induced by scattering of 399 nm light is at least partially counteracted. The solid lines serve as a guide to the eye. Inset: Comparison to an uncooled cloud (gray) that exhibits full atom loss after $\simeq 10 \text{ ms}$.

To obtain a more precise result for the $m_{J'} = 0$ magic angle, we scan the lattice depth for various magnetic field angles. This results in linearly in- or decreasing resonance shifts as depicted in Fig. 2(b), such that we can use the fitted slopes to obtain the zero crossing of the total light shift at $\theta_{\text{magic}} = 38.5(9)^\circ$ [Fig. 2(c)]. Here, we make use of the vanishingly small curvature of the expected functional form in Eq. (1) and use a simple linear fit for this result. While this fit yields a statistical uncertainty on the mrad level, the reported uncertainty is governed by systematic effects, where the dominant contribution stems from the calibration of θ [27].

The magic angle facilitates fast efficient fluorescence imaging via the $^3\text{P}_1$ state by directly collecting fluorescence photons scattered by the cooling light with a high-NA objective [1]. In this work, we instead apply an additional weak probe beam of 399 nm photons for imaging on the $^1\text{P}_1$ state ($I \simeq 10^{-3} I_{\text{sat}}$), which will be crucial for achieving single-site resolution in the retro-reflected clock-magic lattice with a small lattice constant of only 380 nm. To counteract the resulting heating we perform molasses cooling with the horizontal MOT beams at an intensity of $I \simeq I_{\text{sat}}$ and a detuning of $\delta \simeq -20 \text{ kHz}$ from the free-space resonance [Fig. 3]. In the 3D lattice geometry, we find an overall improved loading rate from the MOT for a horizontal polarization of the vertical lattice beams, which we attribute to a larger interference contrast and, thus, a stronger vertical confinement. As a result, a simultaneous magic condition for all three lattice beams cannot be achieved. Nonetheless, we observe that we can reach a quasi-magic condition for all three lattice beams by also adjusting the azimuthal magnetic field angle ϕ [Fig. 3(b)]. This way, we find a contour on which the total number of photon counts for a constant exposure time remains close to the maximum, indicating efficient cooling conditions. The contour can be understood as the light shift introduced by the horizontal lattice being approximately canceled by an opposite light shift from the vertical lattice, with additional effects stemming from the sizeable

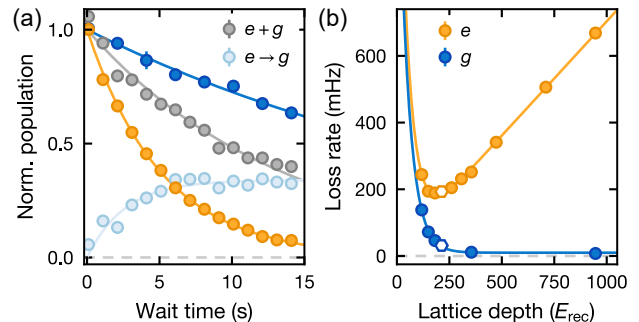


FIG. 4. **$^3\text{P}_0$ clock-state lifetime.** (a) Lifetime of sideband-cooled atoms in a $220 E_{\text{rec}}$ deep 2D lattice initialized in the $^1\text{S}_0$ state (dark blue) or $^3\text{P}_0$ state (orange). Raman-scattering-induced losses out of $^3\text{P}_0$ partially reappear in the $^1\text{S}_0$ state and can be detected from the total atom number (gray) via the difference to the $^3\text{P}_0$ decay curve, yielding the number of converted atoms (light blue). The data is fitted with solutions to coupled differential equations (solid lines), extracting the lifetimes of each state and the fraction of atoms converted through the aforementioned Raman channel [44]. Error bars correspond to the standard error of the mean of three averages. (b) While the ground-state loss rate benefits from deep lattices, Raman losses lead to a linear increase in the $^3\text{P}_0$ clock-state loss rate for lattice depths $\gtrsim 250 E_{\text{rec}}$. Below the optimal trap depth of $220 E_{\text{rec}}$ (white hexagon), strong inelastic collisions and spilling losses start to become dominant. Error bars from the exponential fit uncertainties are smaller than the datapoints, and the solid lines are exponential fits ($^1\text{S}_0$) in combination with a linear term ($^3\text{P}_0$).

electric field splitting compared to the modest external magnetic field strength of 1.3 G [27]. We further note that even for a subpar field orientation a large fraction of atoms remains cooled, whereas the photon count without cooling already saturates at $\simeq 10 \text{ ms}$ due to complete scattering-induced atom loss, as can be seen in Fig. 3(c), inset. Using an exposure time

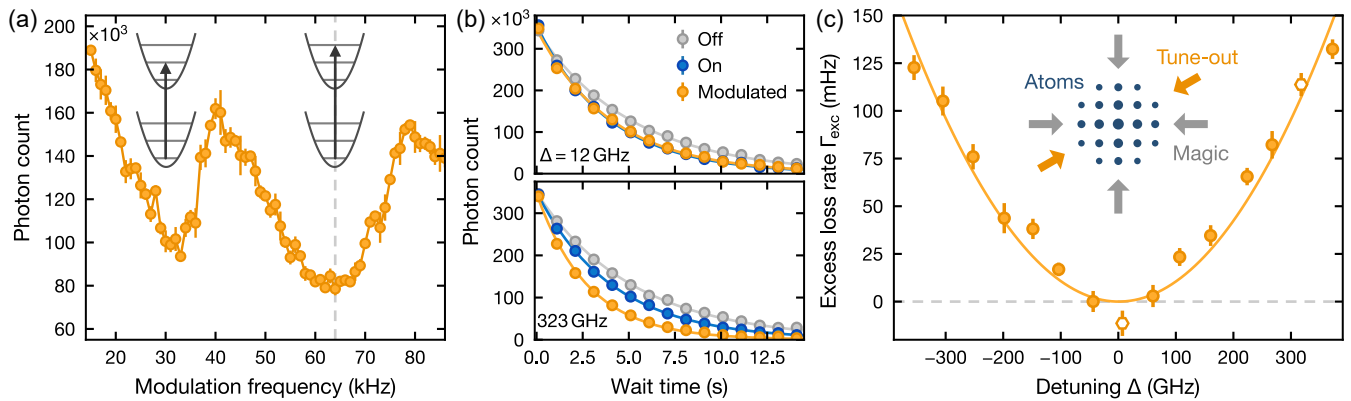


FIG. 5. **Determination of the 3P_0 clock-state tune-out wavelength.** (a) Modulation spectroscopy of clock-state atoms $\simeq 1$ THz detuned from the tune-out wavelength. After 1.5 s of amplitude modulation strong loss features can be found at the longitudinal trap frequency of $\simeq 32$ kHz and its first multiple, with the former corresponding to excitations by one and the latter by two harmonic oscillator quanta (insets). The solid line is a linear interpolation. (b) Clock-state lifetimes in the bare clock-magic lattice (gray), with the additional tune-out lattice at constant amplitude (blue), and with amplitude modulation at $f_{\text{mod}} = 64$ kHz [orange, gray dotted line in (a)]. While the presence of the tune-out lattice induces a moderate, constant excess loss, the modulation leads to pronounced losses for large detunings from the tune-out wavelength (bottom panel) and does not affect the lifetime close to it (top panel). We fit the data with single exponential functions (solid lines). The error bars obtained from three averages are smaller than the datapoints. (c) Excess loss rate from modulation compared to the static tune-out lattice case for varying laser frequencies [white markers indicate the parameters used for the measurements in (b)]. The data follows a quadratic trend (solid line). The error bars are obtained from the standard deviation of the individual lifetime fit uncertainties. Inset: Sketch of the total lattice geometry, with the tune-out lattice at an arbitrarily chosen angle of $\simeq 30^\circ$ with respect to the magic 2D lattice.

of 200 ms, we can thus collect $16\times$ more fluorescence photons per atom on the camera than without cooling, allowing us to resolve atom number variations on the order of 100 atoms.

To study the lifetime of atoms in the 3P_0 state, we apply a resonant, $\simeq 260$ μs long clock π -pulse, followed by a strong 399 nm pulse to remove all atoms that were not transferred to the metastable state and a repump pulse before starting the fluorescence imaging sequence [27]. By varying the wait time between the clock-excitation and repump pulse we can therefore trace the 3P_0 loss rate. In contrast to the ground state, where vacuum losses are typically predominant, off-resonant Raman scattering of 759 nm trap photons limits the 3P_0 lifetime in deep traps [44]. Hence, the tune-out measurement has to be performed in a weak lattice to achieve the best resolution for the heating-induced excess loss rate measurements. To mitigate spilling and two-body inelastic collisions due to atoms occupying higher vibrational bands that can tunnel fast in a shallow optical lattice, we perform cooling prior to the measurement scheme described above. Since this work employs spinless, bosonic ^{174}Yb , cooling techniques that leverage the existence of multiple ground states, such as Λ -enhanced gray molasses or Raman sideband cooling [45–50], are out of reach. Instead, we utilize resolved sideband cooling on the clock transition similar to Ref. [51], which we adapt for use in a 2D lattice [27, 38]. We note that horizontal cooling in a pure 2D lattice is sufficient to localize and separate the atoms well, while the third direction can remain uncooled. After clock-sideband cooling we obtain a mean motional occupation number of $\bar{n} \simeq 0.1$ along each horizontal direction in a $\simeq 220 E_{\text{rec}}$ deep lattice. This enhances the 3P_0 -state lifetime to $\tau = 5.2(1)$ s, which is defined as the $1/e$ -decay time extracted with an exponential fit [Fig. 4(a)]. This lifetime is

still limited by Raman scattering as evidenced by the substantially shorter lifetime of the 3P_0 state compared to that of 1S_0 , and the crossover to a linear increase of the 3P_0 loss rate for deep lattices [Fig. 4(b)]. For shallow lattice depths, strong inelastic collisions and spilling losses increase the loss rate of both 1S_0 and 3P_0 states. A fraction of Raman-scattered atoms from the 3P_0 state reappears in the 1S_0 ground state by decaying via the intermediate 3P_1 state, while atoms scattered to the 3P_2 state are anti-trapped and subsequently lost. The former pathway can be detected by measuring the total atom number, i.e., by omitting from the detection sequence a dedicated resonant pulse that normally removes any 1S_0 atoms. The observed fraction is consistent with the results reported in Ref. [44].

As a next step, while the magic lattice remains in a 2D geometry, superimposing a retro-reflected lattice close to the tune-out wavelength at an arbitrarily chosen angle of $\simeq 30^\circ$ to the 2D lattice enables us to probe sinusoidal amplitude-modulation-induced parametric heating. Similar to the 1D lattice case utilized in previous experiments [26, 29], the incommensurability of wavelengths then incurs mostly phase modulation for atoms in certain lattice sites, while others predominantly experience amplitude modulation as shown in Fig. 5(a), where the modulation spectrum displays two strong resonances at the longitudinal trap frequency and its first multiple. We note that a pure phase modulation from a running wave induced by two detuned beams would provide a stronger single resonance, however, at the expense of a four times lower peak intensity. Choosing the modulation frequency of 64 kHz that shows the strongest loss response, we study the effect of the tune-out lattice on the clock-state lifetime as a function of the laser frequency [Fig. 5(b)]. As can be expected from the negligibly small curvature of the 3P_0 polarizability within

the tuning range and from simple perturbation theory calculations [29, 52], the modulation-induced excess loss rate scales quadratically around the tune-out frequency [Fig. 5(c)]. However, this simple model breaks down for very fast loss dynamics. Here, we observe the emergence of additional, slower timescales arising in the lifetime curves, where the separation into mostly phase- and amplitude-modulated lattice sites and the strong dependence of tunneling rates on the harmonic oscillator state starts to play a role. We therefore restrict the analysis to data that is well described by a single exponential function and perform each measurement at three different average tune-out lattice powers [27]. Computing the weighted mean of the resulting minima then yields a 3P_0 tune-out frequency of

$$f_{\text{to}} = 519.9199 \pm 29_{\text{stat}} \left(\begin{smallmatrix} +57 \\ -45 \end{smallmatrix} \right)_{\text{sys}} \text{ THz.} \quad (2)$$

Here, the statistical uncertainty corresponds to the standard error of the mean, while for the systematic uncertainty we take the deviation from the perturbative regime into account by fitting both the limited and the full dataset with an empirical function that includes a smooth crossover to a linear regime for large detunings [27].

We can compare the measured tune-out wavelength value to the empirical model presented in Ref. [26] and find excellent agreement. Including f_{to} in the model therefore leads to marginal changes of the fit parameters [27]. Leveraging the vanishing 3P_0 polarizability at f_{to} , we further measure the ac Stark shift of the ground state by means of high-resolution clock spectroscopy in the presence of a static, unreflected dipole beam at the tune-out wavelength for varying powers. Repeating this measurement after tuning the laser to the clock transition enables a direct comparison of the relative light shift ratio, which we quantify to be $\Delta\alpha_{\text{to}}/\Delta\alpha_{\text{clock}} = 1.014(11)$. Together with the previously determined clock probe shift of $15(3) \text{ Hz}/(\text{W}/\text{cm}^2)$ reported in Ref. [53], we thus find the empirical model's prediction for the 1S_0 polarizability at the tune-out wavelength of $V_{\text{ac}}/I = -13.0 \text{ h Hz}/(\text{W}/\text{cm}^2)$ to be well within the error bar.

Notably, the presence of the tune-out beam leads to enhanced losses from off-resonant Raman processes, which however do not vary over the chosen detuning range and thus yield a constant offset to the lifetime in the bare 2D lattice. Utilizing the light shift measurement reported above as an intensity calibration [27], we measure the Raman loss rate to be

$12(3) \times 10^{-6} \text{ Hz}/(\text{W}/\text{cm}^2)$, which reasonably agrees with a theoretical estimate of $10.2 \times 10^{-6} \text{ Hz}/(\text{W}/\text{cm}^2)$ [27, 44].

III. SUMMARY AND CONCLUSION

In this work we have presented the first measurement of a metastable excited-state tune-out wavelength, aided by a combination of sideband cooling on the $^1S_0 \rightarrow ^3P_0$ and molasses cooling on the $^1S_0 \rightarrow ^3P_1$ transition. For the latter, we have identified a novel magic angle that allows for triple-magic operation at 759 nm trap light with bosonic ^{174}Yb atoms and characterized a stability region of effective cooling during fluorescence imaging in a 3D clock-magic lattice. This represents a major step towards the realization of an Yb quantum gas microscope with a clock-magic lattice, while the newly determined tune-out wavelength greatly enriches the toolbox for applications in quantum computing and simulation. In particular, tune-out wavelengths may be beneficial for rearrangement of atoms in dense arrays or lattices. Here, one can utilize the ability to apply local light shifts to selectively shelve atoms to the metastable clock state with minimal impact on their coherence as well as to shuttle ground-state atoms to the desired final position without disturbing the potential of shelved atoms, enhancing the scalability of existing quantum computation schemes [1, 18, 43]. Moreover, the triple-magic condition for 3P_1 and 3P_0 in a short-spacing retro-reflected lattice offers exciting opportunities for the realization of novel light-matter interfaces in extreme sub-wavelength arrays [54–56].

ACKNOWLEDGMENTS

This project has received funding from the Deutsche Forschungsgemeinschaft (DFG, German Research Foundation) under Germany's Excellence Strategy – EXC-2111 – 390814868 and via Research Unit FOR5522 under project number 499180199. We further acknowledge funding from the European Research Council (ERC) under the European Union's Horizon 2020 research and innovation program (grant agreement No. 803047), from the German Federal Ministry of Education and Research (BMBF) via the funding program quantum technologies – from basic research to market (contract number 13N15895 FermiQP) and from the Initiative *Munich Quantum Valley* from the State Ministry for Science and the Arts as part of the High-Tech Agenda Plus of the Bavarian State Government. This work has further received funding under Horizon Europe programme HORIZON-CL4-2022-QUANTUM-02-SGA via the project 101113690 (PASQuanS2.1).

[1] J. W. Lis, A. Senoo, W. F. McGrew, F. Rönchen, A. Jenkins, and A. M. Kaufman, Midcircuit Operations Using the *omg* Architecture in Neutral Atom Arrays, *Phys. Rev. X* **13**, 041035 (2023).

[2] S. Ma, G. Liu, P. Peng, B. Zhang, S. Jandura, J. Claes, A. P. Burgers, G. Pupillo, S. Puri, and J. D. Thompson, High-fidelity gates and mid-circuit erasure conversion in an atomic qubit, *Nature* **622**, 279 (2023).

- [3] W. Huie, L. Li, N. Chen, X. Hu, Z. Jia, W. K. C. Sun, and J. P. Covey, Repetitive Readout and Real-Time Control of Nuclear Spin Qubits in ^{171}Yb Atoms, *PRX Quantum* **4**, 030337 (2023).
- [4] B. W. Reichardt, A. Paetznick, D. Aasen, I. Basov, J. M. Bello-Rivas, P. Bonderson, R. Chao, W. van Dam, M. B. Hastings, A. Paz, M. P. da Silva, A. Sundaram, K. M. Svore, A. Vashillo, Z. Wang, M. Zanner, W. B. Cairncross, C.-A. Chen, D. Crow, H. Kim, J. M. Kindem, J. King, M. McDonald, M. A. Norcia, A. Ryou, M. Stone, L. Wadleigh, K. Barnes, P. Battaglino, T. C. Bohdanowicz, G. Booth, A. Brown, M. O. Brown, K. Cassella, R. Coxe, J. M. Epstein, M. Feldkamp, C. Griger, E. Halperin, A. Heinz, F. Hummel, M. Jaffe, A. M. W. Jones, E. Kapit, K. Kotru, J. Lauigan, M. Li, J. Marjanovic, E. Megidish, M. Meredith, R. Morshead, J. A. Muniz, S. Narayanaswami, C. Nishiguchi, T. Paule, K. A. Pawlak, K. L. Pudenz, D. R. Pérez, J. Simon, A. Smull, D. Stack, M. Urbanek, R. J. M. van de Veerdonk, Z. Vendeiro, R. T. Weverka, T. Wilkason, T.-Y. Wu, X. Xie, E. Zalys-Geller, X. Zhang, and B. J. Bloom, Logical computation demonstrated with a neutral atom quantum processor (2024), [arXiv:2411.11822](https://arxiv.org/abs/2411.11822).
- [5] F. Scazza, C. Hofrichter, M. Höfer, P. C. De Groot, I. Bloch, and S. Fölling, Observation of two-orbital spin-exchange interactions with ultracold $\text{SU}(N)$ -symmetric fermions, *Nat. Phys.* **10**, 779 (2014).
- [6] G. Pagano, M. Mancini, G. Cappellini, P. Lombardi, F. Schäfer, H. Hu, X.-J. Liu, J. Catani, C. Sias, M. Inguscio, and L. Fallani, A one-dimensional liquid of fermions with tunable spin, *Nat. Phys.* **10**, 198 (2014).
- [7] S. Taie, E. Ibarra-García-Padilla, N. Nishizawa, Y. Takasu, Y. Kuno, H.-T. Wei, R. T. Scalettar, K. R. Hazzard, and Y. Takahashi, Observation of antiferromagnetic correlations in an ultracold $\text{SU}(N)$ Hubbard model, *Nat. Phys.* **18**, 1356 (2022).
- [8] G. Pasqualetti, O. Bettermann, N. Darkwah Oppong, E. Ibarra-García-Padilla, S. Dasgupta, R. T. Scalettar, K. R. A. Hazzard, I. Bloch, and S. Fölling, Equation of State and Thermometry of the 2D $\text{SU}(N)$ Fermi-Hubbard Model, *Phys. Rev. Lett.* **132**, 083401 (2024).
- [9] J. Ye, H. J. Kimble, and H. Katori, Quantum State Engineering and Precision Metrology Using State-Insensitive Light Traps, *Science* **320**, 1734 (2008).
- [10] A. D. Ludlow, M. M. Boyd, J. Ye, E. Peik, and P. Schmidt, Optical atomic clocks, *Rev. Mod. Phys.* **87**, 637 (2015).
- [11] A. Aepli, K. Kim, W. Warfield, M. S. Safronova, and J. Ye, Clock with 8×10^{-19} Systematic Uncertainty, *Phys. Rev. Lett.* **133**, 023401 (2024).
- [12] A. Cao, W. J. Eckner, T. Lukin Yelin, A. W. Young, S. Jandura, L. Yan, K. Kim, G. Pupillo, J. Ye, N. Darkwah Oppong, and A. M. Kaufman, Multi-qubit gates and Schrödinger cat states in an optical clock, *Nature* **634**, 315 (2024).
- [13] S. Kolkowitz, S. Bromley, T. Bothwell, M. Wall, G. Marti, A. Koller, X. Zhang, A. Rey, and J. Ye, Spin-orbit-coupled fermions in an optical lattice clock, *Nature* **542**, 66 (2017).
- [14] M. Mancini, G. Pagano, G. Cappellini, L. Livi, M. Rider, J. Catani, C. Sias, P. Zoller, M. Inguscio, M. Dalmonte, and L. Fallani, Observation of chiral edge states with neutral fermions in synthetic Hall ribbons, *Science* **349**, 1510 (2015).
- [15] T. W. Zhou, T. Beller, G. Masini, J. Parravicini, G. Cappellini, C. Repellin, T. Giamarchi, J. Catani, M. Filippone, and L. Fallani, Measuring Hall voltage and Hall resistance in an atom-based quantum simulator (2024), [arXiv:2411.09744](https://arxiv.org/abs/2411.09744).
- [16] Z. W. Barber, J. E. Stalnaker, N. D. Lemke, N. Poli, C. W. Oates, T. M. Fortier, S. A. Diddams, L. Hollberg, C. W. Hoyt, A. V. Taichenachev, and V. I. Yudin, Optical Lattice Induced Light Shifts in an Yb Atomic Clock, *Phys. Rev. Lett.* **100**, 103002 (2008).
- [17] C. Chen, G. Bornet, M. Bintz, G. Emperauger, L. Leclerc, V. S. Liu, P. Scholl, D. Barredo, J. Hauschild, S. Chatterjee, M. Schuler, A. Läuchli, M. P. Zaletel, T. Lahaye, N. Y. Yao, and A. Browaeys, Continuous symmetry breaking in a two-dimensional Rydberg array, *Nature* **616**, 691 (2023).
- [18] D. Bluvstein, S. J. Evered, A. A. Geim, S. H. Li, H. Zhou, T. Manovitz, S. Ebadi, M. Cain, M. Kalinowski, D. Hangleiter, J. P. Bonilla Ataides, N. Maskara, I. Cong, X. Gao, P. Sales Rodriguez, T. Karolyshyn, G. Semeghini, M. J. Gullans, M. Greiner, V. Vuletić, and M. D. Lukin, Logical quantum processor based on reconfigurable atom arrays, *Nature* **626**, 58 (2024).
- [19] N. Darkwah Oppong, G. Pasqualetti, O. Bettermann, P. Zechmann, M. Knap, I. Bloch, and S. Fölling, Probing Transport and Slow Relaxation in the Mass-Imbalanced Fermi-Hubbard Model, *Phys. Rev. X* **12**, 031026 (2022).
- [20] F. M. Surace, P. Fromholz, N. Darkwah Oppong, M. Dalmonte, and M. Aidelsburger, *Ab Initio* Derivation of Lattice-Gauge-Theory Dynamics for Cold Gases in Optical Lattices, *PRX Quantum* **4**, 020330 (2023).
- [21] A. González-Tudela and J. I. Cirac, Cold atoms in twisted-bilayer optical potentials, *Phys. Rev. A* **100**, 053604 (2019).
- [22] X.-W. Luo and C. Zhang, Spin-Twisted Optical Lattices: Tunable Flat Bands and Larkin-Ovchinnikov Superfluids, *Phys. Rev. Lett.* **126**, 103201 (2021).
- [23] G. Pagano, F. Scazza, and M. Foss-Feig, Fast and Scalable Quantum Information Processing with Two-Electron Atoms in Optical Tweezer Arrays, *Adv. Quantum Tech.* **2**, 1800067 (2019).
- [24] A. J. Daley, M. M. Boyd, J. Ye, and P. Zoller, Quantum Computing with Alkaline-Earth-Metal Atoms, *Phys. Rev. Lett.* **101**, 170504 (2008).
- [25] D. González-Cuadra, D. Bluvstein, M. Kalinowski, R. Kaubuegger, N. Maskara, P. Naldesi, T. V. Zache, A. M. Kaufman, M. D. Lukin, H. Pichler, B. Vermersch, J. Ye, and P. Zoller, Fermionic quantum processing with programmable neutral atom arrays, [arXiv:2303.06985](https://arxiv.org/abs/2303.06985) (2023).
- [26] T. O. Höhn, E. Staub, G. Brochier, N. Darkwah Oppong, and M. Aidelsburger, State-dependent potentials for the 1S_0 and 3P_0 clock states of neutral ytterbium atoms, *Phys. Rev. A* **108**, 053325 (2023).
- [27] See Supplemental Material which includes Refs. [57–60], for additional information about the experimental setup and sequences, the initial state characterization, read-out techniques, additional data and error analysis for the magic angle and tune-out measurements, experimental results on the Raman scattering rate and the differential light shift at f_{to} and at the clock resonance, and a discussion of the expanded empirical polarizability model.
- [28] M. S. Safronova, Z. Zuhrianda, U. I. Safronova, and C. W. Clark, Extracting transition rates from zero-polarizability spectroscopy, *Phys. Rev. A* **92**, 040501 (2015).
- [29] A. Heinz, A. J. Park, N. Šantić, J. Trautmann, S. G. Porsev, M. S. Safronova, I. Bloch, and S. Blatt, State-Dependent Optical Lattices for the Strontium Optical Qubit, *Phys. Rev. Lett.* **124**, 203201 (2020).
- [30] L. Franchi, L. F. Livi, G. Cappellini, G. Binella, M. Inguscio, J. Catani, and L. Fallani, State-dependent interactions in ultracold ^{174}Yb probed by optical clock spectroscopy, *New J. Phys.* **19**, 103037 (2017).
- [31] R. Bouganne, M. B. Aguilera, A. Dureau, E. Soave, J. Beugnon, and F. Gerbier, Clock spectroscopy of interacting bosons in deep optical lattices, *New J. Phys.* **19**, 113006 (2017).

- [32] C. D. Herold, V. D. Vaidya, X. Li, S. L. Rolston, J. V. Porto, and M. S. Safronova, Precision Measurement of Transition Matrix Elements via Light Shift Cancellation, *Phys. Rev. Lett.* **109**, 243003 (2012).
- [33] A. Ratkuta, P. D. Gregory, A. D. Innes, J. A. Matthies, L. A. McArd, J. M. Mortlock, M. S. Safronova, S. L. Bromley, and S. L. Cornish, Measurement of the tune-out wavelength for ^{133}Cs at 880 nm, *Phys. Rev. A* **104**, 052813 (2021).
- [34] F. Schmidt, D. Mayer, M. Hohmann, T. Lausch, F. Kindermann, and A. Widera, Precision measurement of the ^{87}Rb tune-out wavelength in the hyperfine ground state $F = 1$ at 790 nm, *Phys. Rev. A* **93**, 022507 (2016).
- [35] W. Kao, Y. Tang, N. Q. Burdick, and B. L. Lev, Anisotropic dependence of tune-out wavelength near Dy 741-nm transition, *Opt. Express* **25**, 3411 (2017).
- [36] J. Catani, G. Barontini, G. L'amporesi, F. Rabatti, G. Thalhammer, F. Minardi, S. Stringari, and M. Inguscio, Entropy Exchange in a Mixture of Ultracold Atoms, *Phys. Rev. Lett.* **103**, 140401 (2009).
- [37] S. Dörscher, R. Schwarz, A. Al-Masoudi, S. Falke, U. Sterr, and C. Lisdat, Lattice-induced photon scattering in an optical lattice clock, *Phys. Rev. A* **97**, 063419 (2018).
- [38] R. M. Kroeze, T. O. Höhn, R. A. Villela, E. Zu, and M. Aidelsburger, Clock sideband cooling of ytterbium to the 3D motional ground state, in preparation.
- [39] R. Yamamoto, J. Kobayashi, T. Kuno, K. Kato, and Y. Takahashi, An ytterbium quantum gas microscope with narrow-line laser cooling, *New J. Phys.* **18**, 023016 (2016).
- [40] A. Jenkins, J. W. Lis, A. Senoo, W. F. McGrew, and A. M. Kaufman, Ytterbium Nuclear-Spin Qubits in an Optical Tweezer Array, *Phys. Rev. X* **12**, 021027 (2022).
- [41] S. Ma, A. P. Burgers, G. Liu, J. Wilson, B. Zhang, and J. D. Thompson, Universal Gate Operations on Nuclear Spin Qubits in an Optical Tweezer Array of ^{171}Yb Atoms, *Phys. Rev. X* **12**, 021028 (2022).
- [42] M. A. Norcia, W. B. Cairncross, K. Barnes, P. Battaglino, A. Brown, M. O. Brown, K. Cassella, C.-A. Chen, R. Coxe, D. Crow, J. Epstein, C. Griger, A. M. W. Jones, H. Kim, J. M. Kindem, J. King, S. S. Kondov, K. Kotru, J. Lauigan, M. Li, M. Lu, E. Megidish, J. Marjanovic, M. McDonald, T. Mittiga, J. A. Muniz, S. Narayanaswami, C. Nishiguchi, R. Notermans, T. Paule, K. A. Pawlak, L. S. Peng, A. Ryou, A. Smull, D. Stack, M. Stone, A. Sucich, M. Urbanek, R. J. M. van de Veerdonk, Z. Vendeiro, T. Wilkason, T.-Y. Wu, X. Xie, X. Zhang, and B. J. Bloom, Midcircuit Qubit Measurement and Rearrangement in a ^{171}Yb Atomic Array, *Phys. Rev. X* **13**, 041034 (2023).
- [43] M. A. Norcia, H. Kim, W. B. Cairncross, M. Stone, A. Ryou, M. Jaffe, M. O. Brown, K. Barnes, P. Battaglino, T. C. Bohdanowicz, A. Brown, K. Cassella, C. A. Chen, R. Coxe, D. Crow, J. Epstein, C. Griger, E. Halperin, F. Hummel, A. M. W. Jones, J. M. Kindem, J. King, K. Kotru, J. Lauigan, M. Li, M. Lu, E. Megidish, J. Marjanovic, M. McDonald, T. Mittiga, J. A. Muniz, S. Narayanaswami, C. Nishiguchi, T. Paule, K. A. Pawlak, L. S. Peng, K. L. Pudenz, D. R. Perez, A. Smull, D. Stack, M. Urbanek, R. J. M. van de Veerdonk, Z. Vendeiro, L. Wadleigh, T. Wilkason, T. Y. Wu, X. Xie, E. Zaly-Geller, X. Zhang, and B. J. Bloom, Iterative assembly of ^{171}Yb atom arrays in cavity-enhanced optical lattices (2024), [arXiv:2401.16177](https://arxiv.org/abs/2401.16177).
- [44] J. L. Siegel, W. F. McGrew, Y. S. Hassan, C.-C. Chen, K. Beloy, T. Grogan, X. Zhang, and A. D. Ludlow, Excited-Band Coherent Delocalization for Improved Optical Lattice Clock Performance, *Phys. Rev. Lett.* **132**, 133201 (2024).
- [45] J. Ang'ong'a, C. Huang, J. P. Covey, and B. Gadway, Gray molasses cooling of ^{39}K atoms in optical tweezers, *Phys. Rev. Res.* **4**, 013240 (2022).
- [46] A. T. Grier, I. Ferrier-Barbut, B. S. Rem, M. Delehay, L. Khaykovich, F. Chevy, and C. Salomon, Λ -enhanced sub-doppler cooling of lithium atoms in D_1 gray molasses, *Phys. Rev. A* **87**, 063411 (2013).
- [47] A. M. Kaufman, B. J. Lester, and C. A. Regal, Cooling a Single Atom in an Optical Tweezer to Its Quantum Ground State, *Phys. Rev. X* **2**, 041014 (2012).
- [48] J. D. Thompson, T. G. Tiecke, A. S. Zibrov, V. Vuletić, and M. D. Lukin, Coherence and Raman Sideband Cooling of a Single Atom in an Optical Tweezer, *Phys. Rev. Lett.* **110**, 133001 (2013).
- [49] S. E. Hamann, D. L. Haycock, G. Klose, P. H. Pax, I. H. Deutsch, and P. S. Jessen, Resolved-Sideband Raman Cooling to the Ground State of an Optical Lattice, *Phys. Rev. Lett.* **80**, 4149 (1998).
- [50] A. J. Kerman, *Raman sideband cooling and cold atomic collisions in optical lattices*, Ph.D. thesis, Stanford University, California (2002).
- [51] N. Nemitz, T. Ohkubo, M. Takamoto, I. Ushijima, M. Das, N. Ohmae, and H. Katori, Frequency ratio of Yb and Sr clocks with 5×10^{-17} uncertainty at 150 seconds averaging time, *Nat. Photon.* **10**, 258 (2016).
- [52] T. A. Savard, K. M. O'Hara, and J. E. Thomas, Laser-noise-induced heating in far-off resonance optical traps, *Phys. Rev. A* **56**, R1095 (1997).
- [53] N. Poli, Z. W. Barber, N. D. Lemke, C. W. Oates, L. S. Ma, J. E. Stalnaker, T. M. Fortier, S. A. Diddams, L. Hollberg, J. C. Bergquist, A. Brusch, S. Jefferts, T. Heavner, and T. Parker, Frequency evaluation of the doubly forbidden $^1S_0 \rightarrow ^3P_0$ transition in bosonic ^{174}Yb , *Phys. Rev. A* **77**, 050501 (2008).
- [54] L. Henriot, J. S. Douglas, D. E. Chang, and A. Albrecht, Critical open-system dynamics in a one-dimensional optical-lattice clock, *Phys. Rev. A* **99**, 023802 (2019).
- [55] R. Bekenstein, I. Pikovski, H. Pichler, E. Shahmoon, S. F. Yelin, and M. D. Lukin, Quantum metasurfaces with atom arrays, *Nat. Phys.* **16**, 676 (2020).
- [56] S. J. Masson, J. P. Covey, S. Will, and A. Asenjo-Garcia, Dicke Superradiance in Ordered Arrays of Multilevel Atoms, *PRX Quantum* **5**, 010344 (2024).
- [57] L. Riegger, N. Darkwah Oppong, M. Höfer, D. R. Fernandes, I. Bloch, and S. Fölling, Localized Magnetic Moments with Tunable Spin Exchange in a Gas of Ultracold Fermions, *Phys. Rev. Lett.* **120**, 143601 (2018).
- [58] D. A. Steck, *Quantum and Atom Optics* (2007).
- [59] A. V. Taichenachev, V. I. Yudin, C. W. Oates, C. W. Hoyt, Z. W. Barber, and L. Hollberg, Magnetic Field-Induced Spectroscopy of Forbidden Optical Transitions with Application to Lattice-Based Optical Atomic Clocks, *Phys. Rev. Lett.* **96**, 083001 (2006).
- [60] B. H. Bransden and C. J. Joachain, *Physics of Atoms and Molecules* (Pearson Education, Prentice Hall, New York, 2003).

SUPPLEMENTAL MATERIAL

S.I. EXPERIMENTAL SEQUENCE

Lattice loading: The experiment starts by loading a 3D MOT on the $^1S_0 \rightarrow ^3P_1$ transition for 500 ms, which typically results in a total atom number of $\simeq 4 \times 10^6$. We note that compared to the MOT setup described in Ref. [26], we inserted a high-resolution objective (NA = 0.7), where the bottom MOT beam is now projected onto the back focal plane of the objective. At the beginning of the MOT compression stage, we quench on the 3D clock-magic lattice to $\simeq 330 E_{\text{rec}}$ in each horizontal direction and to $\simeq 720 E_{\text{rec}}$ in the vertical axis. After 50 ms of equilibration time in the lattice while keeping the MOT on, both the MOT beams and the magnetic field gradient are extinguished, and after an additional 25 ms of wait time the vertical lattice is ramped down within 50 ms.

Magic-angle measurement in 2D lattice: For the magic-angle measurements in Fig. 2 of the main text, the 2D lattice is quickly ramped to the desired depth. Spectroscopy is performed using a 500 μs long pulse on the 3P_1 transition, where the light is applied via one of the horizontal MOT beams.

Free-space spectroscopy: For the free-space spectroscopy in Fig. 2 of the main text, the 2D lattice is fully quenched off before applying the 500 μs long spectroscopy pulse and then quenched back on, retaining more than 70% of the atoms.

Lifetime measurements: For the 3P_0 state lifetime presented in Fig. 4 in the main text, we first perform clock-sideband cooling in the 2D lattice, as described in Section S.III. Subsequently, the horizontal lattices are ramped to 110 E_{rec} depth along each direction, followed by resonant clock excitation. Any remnant ground-state atoms are subsequently removed by means of a 3 ms, resonant pulse on the 1P_1 transition, followed by a variable wait time before imaging. The 1S_0 lifetime is measured identically but by omitting the excitation and removal pulses.

Tune-out measurement: For the tune-out measurements in Fig. 5 in the main text, the sequence follows that of the clock state lifetime, with the following modifications. After clock excitation and ground-state atom removal, the tune-out lattice is ramped to the desired intensity over 5 ms. Then, the intensity of the tune-out lattice is either held constant or modulated sinusoidally, for a variable wait time. After the wait, the tune-out lattice is ramped down over 5 ms prior to imaging.

Imaging: When imaging 3P_0 atoms, we first remove any 1S_0 atoms that may have appeared as a result of Raman scattering, identical to how these are removed after clock excitation. Then, all three lattices are ramped up to their maximal depth within 5 ms. We then apply a repump pulse to transfer the clock-state atoms back to the ground state, where they are imaged on the 1P_1 transition while being molasses-cooled using the MOT beams as described in the main text. Imaging of 1S_0 atoms proceeds identically but by omitting the removal and repump pulses.

S.II. EMPIRICAL POLARIZABILITY MODEL

Utilizing the empirical model for the 1S_0 and 3P_0 ac polarizabilities developed in our previous work [26], we obtain only marginal corrections from $\lambda_{\text{eff},^3P_0} = 376.1 \text{ nm}$ to 374.7 nm and from $\Gamma_{\text{eff},^3P_0} = 22.9 \text{ MHz}$ to 23.6 MHz upon inclusion of the newly measured tune-out wavelength at 576.6 nm . This does not lead to visible changes in the polarizability curves, and the benchmark polarizability ratios at 670 nm , 671.5 nm , and 690.1 nm are affected on a level well below the measurement uncertainty [19, 57].

Due to the increasing relevance of state-dependent potentials also for the intercombination line ($^1S_0 \rightarrow ^3P_1$) and a multitude of measured magic wavelengths at specific magic angles [1, 39–43], we extend the polarizability model to the 3P_1 state. We use the general expression for the total light shift [58]

$$V_{\text{ac}}(\omega) = -\frac{I}{2c\epsilon_0} \left[\alpha^{(0)}(\omega) + \alpha^{(1)}(\omega)q(\hat{k} \cdot \hat{z})\frac{m_F}{F} + \alpha^{(2)}(\omega)\frac{3|\hat{\epsilon}_z|^2 - 1}{2}\frac{3m_F^2 - F(F+1)}{F(2F-1)} \right], \quad (\text{S.1})$$

with the scalar, vector, and tensor polarizabilities denoted as $\alpha^{(0,1,2)}$, respectively, the total atomic angular momentum F , the angular frequency of the trapping light ω , its intensity I , unit wave vector \hat{k} , polarization vector $\hat{\epsilon}$, quantization axis \hat{z} , and the degree of circular polarization q . Due to the finite electronic angular momentum, scalar and tensor light shifts are typically comparably strong, while the vector shift vanishes for linearly polarized trapping light ($q = 0$) as is the case in our experiment. The scalar and tensor shifts can be further expressed in terms of the reduced dipole matrix element as [58]

$$\alpha^{(0)}(\omega) = \sum_{F'} \frac{2\omega_{F'F}}{3\hbar(\omega_{F'F}^2 - \omega^2)} |\langle F \parallel \mathbf{d} \parallel F' \rangle|^2 \quad (\text{S.2})$$

and

$$\alpha^{(2)}(\omega) = \sum_{F'} (-1)^{F'+F} \sqrt{\frac{40F(2F+1)(2F-1)}{3(F+1)(2F+3)}} \times \left\{ \begin{matrix} 1 & 1 & 2 \\ F & F & F' \end{matrix} \right\} \frac{\omega_{F'F}}{\hbar(\omega_{F'F}^2 - \omega^2)} |\langle F \parallel \mathbf{d} \parallel F' \rangle|^2, \quad (\text{S.3})$$

which can in turn be linked to the transition linewidths [26].

As with the model for the 3P_0 polarizability, we truncate the set of transitions that are included directly, as shown in Fig. S1, and absorb the neglected higher-lying transitions in an effective line at $\lambda_{\text{eff},^3P_1}$ with width $\Gamma_{\text{eff},^3P_1}$. By accounting for the fine-structure splitting, we directly relate $\lambda_{\text{eff},^3P_1}$ to $\lambda_{\text{eff},^3P_0}$, yielding $\lambda_{\text{eff},^3P_1} = 384.9 \text{ nm}$ and leaving only Γ_{eff} as a free parameter. Furthermore, we take the finite transition strengths to 3D_2 states into account by splitting the linewidth of the effective excited state into two components with $J = 1$ and $J = 2$, respectively. Their corresponding strengths are deduced from the nearby $(6s7d)^3D_1$ and 3D_2 transition strength ratio as a

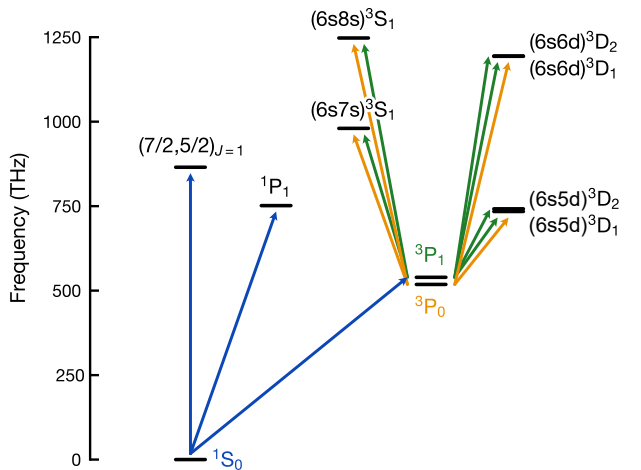


FIG. S1. **Energy levels and transitions used for the empirical polarizability models.** Following the treatment of the 1S_0 and 3P_0 ac polarizabilities in Ref. [26], we use a limited dataset of relevant states to describe the polarizability of the 3P_1 state in the optical spectrum. In addition to the 3S_1 and 3D_1 states that are strongly coupled to 3P_0 , in the case of 3P_1 also transitions to 3D_2 states need to be taken into account.

simplification in order to minimize the number of free parameters. Similarly, the identical resonance frequency can be motivated by the very small fine-structure splitting of the $(6s7d)^3D$ states. Using the magic wavelengths that have been determined for ^{171}Yb [1, 41–43] and our magic angle at 759 nm for ^{174}Yb , we obtain high agreement with our empirical model for a combined effective linewidth of $\Gamma_{\text{eff},^3P_1} \approx 2\pi \times 59$ MHz. We note that the measured scalar and tensor polarizabilities at 532 nm in Ref. [39] cannot be reproduced by our model.

S.III. SIDEBAND COOLING

As described in the main text, we cool the atomic sample to prolong the excited state lifetime. Lower temperatures allow us to use less lattice light to confine the atoms, thereby minimizing the Raman scattering losses discussed in the main text and Sec. S.V. At the same time, reduced temperatures suppress inelastic losses between pairs of excited state atoms. In this Section we briefly outline the general performance and sequence, details on the adaptation of this standard technique to the 2D lattice will be described elsewhere [38].

To perform cooling, atoms are excited on the resolved red sideband of the ultranarrow clock transition $^1S_0 \rightarrow ^3P_0$ [51]. The cooling cycle is closed by repumping on the $^3P_0 \rightarrow ^3D_1$ transition, which decays via 3P_1 back to the ground state 1S_0 , as described in the main text and S.I. We choose this repumping transition because of the reasonably short radiative lifetime of ≈ 300 ns, the favorable branching ratios with only marginal, $\approx 3\%$ losses into the dark and anti-trapped 3P_2 state, and the long wavelength of 1389 nm, resulting in a low recoil energy of $h \times 595$ Hz.

Cooling is performed in a 2D lattice configuration, where

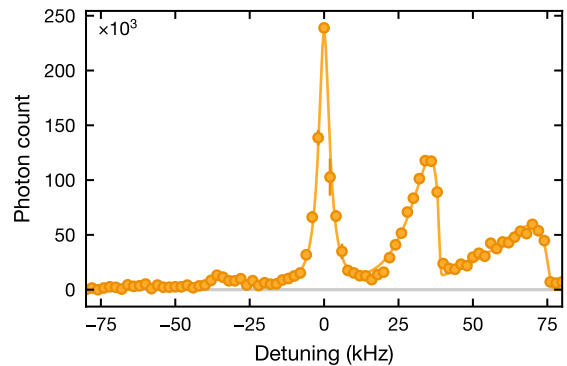


FIG. S2. **Sideband spectroscopy after clock-sideband cooling in a 2D lattice.** Resolved sideband spectrum in a balanced, 2D lattice with $\approx 220E_{\text{rec}}$ combined depth. The figure shows the first two red and blue sidebands, where the second red sideband is fully suppressed and a small fraction of the first red sideband is still visible. Error bars correspond to the standard error of the mean over three averages. The solid line is a guide to the eye.

the two lattices are matched in depth to $\approx 330 E_{\text{rec}}$ each. Two clock beams, each (approximately) co-propagating with one of the lattices, are used to drive separate pulses on the red sideband transition. The sideband pulse duration is limited by the achievable clock Rabi rate for which we use a strong magnetic field of ≈ 400 G to induce the clock transition [59]. Together with ~ 100 mW of power, each beam reaches a carrier transition Rabi rate of $\Omega \approx 2\pi \times 3.2$ kHz. We send 15 clock cooling pulses with 1 ms duration, each followed by a 500 μs repumping pulse. To efficiently address all atoms in the 2D lattice, the frequency of the clock beams is swept during this time from -30 kHz to -72 kHz to address inhomogeneities in the sideband frequency [38]. This sequence is then repeated along the other direction to complete one cooling “cycle”, and we perform 10 such cooling cycles. Prior to cooling, time-of-flight expansion reveals the atoms to have a temperature of $T_{\text{hor}} \approx 10$ μK ($\bar{n} \approx 2.6$). After cooling, this temperature is reduced to $T_{\text{hor}} \approx 1.6$ μK ($\bar{n} \approx 0.15$) as determined using sideband spectroscopy. The spectroscopy utilizes a 30 ms long clock pulse with $\Omega \approx 2\pi \times 2.1$ kHz, ensuring that the transition is incoherently driven. Figure S2 shows the sideband spectrum after the subsequent adiabatic ramp of the lattice depth to that yielding maximal lifetime, i.e. $\approx 220 E_{\text{rec}}$. In that lattice, the thermal occupation results in an average hopping rate of ≈ 150 mHz compared to ≈ 170 Hz prior to cooling.

We note that the vertical direction is not explicitly cooled. After application of a coherent clock π -pulse we observe rapid (≈ 5 ms) losses of $\sim 40\%$ of the 3P_0 atoms. We ascribe this to inelastic collisions between multiple 3P_0 atoms residing on a single lattice site facilitated by the high temperature along the weakly confined vertical direction. Indeed, we confirm that a larger particle density results in more severe losses. Adding vertical confinement inhibits these losses, though at the cost of increased Raman scattering, and we opt to accept this rapid initial loss in favor of the longer lifetime. To avoid any effects from these losses affecting the lifetime measurement, we thus

choose a minimal wait time of 100 ms after the application of the clock pulse before we start to record the lifetime. This further ensures that any detrimental effects of the settling of the strong external magnetic field, observed to take ≈ 20 ms, are avoided.

S.IV. INTENSITY CALIBRATION

Determining the intensity of the tune-out beam is a crucial ingredient for an accurate measurement of the Raman scattering rate (Section S.V). To this end, we tune the laser to be resonant with the clock transition and illuminate the atomic sample with a dipole beam (retro-reflection is blocked). Moreover, we work at low optical power $P \leq 10$ mW to limit power broadening. This way, we measure an ac Stark shift response of 98.0(6) kHz/W. Utilizing the experimentally determined polarizability reported in Ref. [53] and the carefully calibrated total power of the dipole beam, we obtain a waist of 99(10) μ m. We then set the laser frequency to the tune-out value and repeat the spectroscopy measurements using the same settings. We obtain a response of 99.3(8) kHz/W, which we use to compute the relative light shift of $\Delta\alpha_{\text{to}}/\Delta\alpha_{\text{clock}} = 1.014(11)$ as mentioned in the main text.

S.V. RAMAN SCATTERING

Both the magic wavelength lattice and the tune-out light induce Raman scattering which results in additional loss of $^3\text{P}_0$ atoms. For the wavelengths and intensities employed here, the Raman scattering mechanism dominates over other loss mechanisms such as vacuum-limited collisions, spontaneous emission and black body radiation. Raman scattering out of the $^3\text{P}_0$ state predominantly results in decay to the other fine-structure states, i.e., $^3\text{P}_1$ and $^3\text{P}_2$. While atoms in the $^3\text{P}_1$ state quickly decay back to the ground state $^1\text{S}_0$ and can be detected as shown in Fig. 4 in the main text, the $^3\text{P}_2$ state is long-lived and anti-trapped by the clock-magic lattice, resulting in loss of the $^3\text{P}_2$ population.

In this Section we provide a quantitative analysis of the observed Raman scattering and details of the theoretical calculation of the expected scattering rates.

A. Experiment

As shown in Fig. 5 of the main text, the presence of a constant, i.e. non-modulated, tune-out lattice results in excess loss of atoms out of the $^3\text{P}_0$ state. Fig. S4(d) shows that this excess loss is independent of laser frequency over the range explored in this work, and that it is linearly proportional to the intensity as expected for Raman scattering. To quantitatively analyze the Raman scattering induced by the tune-out light, we block the retro-reflecting mirror resulting in a dipole trap rather than an optical lattice. This simplifies the analysis as systematic effects such as imperfect lattice alignment are eliminated.

The excess loss rate observed in this configuration is shown in Fig. S3(a). Together with the intensity calibration described in Sec. S.IV, we can accurately extract the relation between Raman loss rate and light shift, yielding $8(1) \times 10^{-7}$ Hz_{loss}/Hz_{lightshift}. While this quantity is practically useful, it does not enable comparison to theoretical calculations. For that, we use the beam waist inferred from the light shift spectroscopy and find $12(3) \times 10^{-6}$ Hz/(W/cm²). We note that again the increased uncertainty is dominated by the measurement of the probe light shift of resonant clock light reported in Ref. [53].

B. Theory

This type of off-resonant scattering rate can be calculated using the Kramers-Heisenberg formula [60]. Assuming a linearly polarized lattice and neglecting the hyperfine interaction, the total scattering rate $\Gamma_{i \rightarrow f}(\omega)$ from initial state i to final state f induced by radiation of angular frequency ω and intensity I can be written as [44]

$$\Gamma_{i \rightarrow f}(\omega) = \Lambda_{if} \frac{(\omega - \omega_{fi})^3}{6\pi\epsilon_0^2 c^4 \hbar} |\alpha_{if}(\omega)|^2 I, \quad (\text{S.4})$$

where the branching ratio (after summing over the hyperfine substates) $\Lambda_{if} = 1$ for all our transitions of interest, $\hbar\omega_{fi}$ is the splitting between states i and f , and

$$\alpha_{if}(\omega) = \sum_k \alpha_{ikf}(\omega) \quad (\text{S.5})$$

sums the contributions over all intermediate states k . We note that while Ref. [44] expresses the scattering rate in terms of trap depth, we instead write it explicitly in terms of the intensity. This is to avoid confusion at tune-out wavelengths, where the former vanishes but the latter remains well-defined.

These calculations, in particular of $\alpha_{ikf}(\omega)$, require accurate knowledge of not only transition frequencies to higher excited states, but also dipole matrix elements. While our empirical polarizability model described in Sec. S.II sufficiently captures the relevant transitions out of $^1\text{S}_0$, $^3\text{P}_0$, and $^3\text{P}_1$, we have not developed a similar model for $^3\text{P}_2$. Instead, we utilize the results of the calculations in Ref. [44] and generalize these to other wavelengths of interest. Specifically, Table I of the Supplemental Material of Ref. [44] reports the quantities $\alpha_{ikf}(\omega_{\text{magic}})$ for $\omega_{\text{magic}} = 2\pi c/\lambda$ with $\lambda = 759.3$ nm. These can be converted to other frequencies using

$$\frac{\alpha_{ikf}(\omega')}{\alpha_{ikf}(\omega)} = \left[\frac{1}{\omega_{ki} - \omega'} + \frac{(-1)^{J_f}}{\omega_{ki} + \omega_{if} + \omega'} \right] \times \left[\frac{1}{\omega_{ki} - \omega} + \frac{(-1)^{J_f}}{\omega_{ki} + \omega_{if} + \omega} \right]^{-1}, \quad (\text{S.6})$$

where we used $\omega_{kf} = \omega_{ki} + \omega_{if}$. This conversion depends solely on the two frequencies ω and ω' , the final state angular momentum $J_f = 1(2)$ for $^3\text{P}_1(^3\text{P}_2)$, the well-known fine-structure splittings ω_{if} and the excitation frequencies ω_{ki} . The

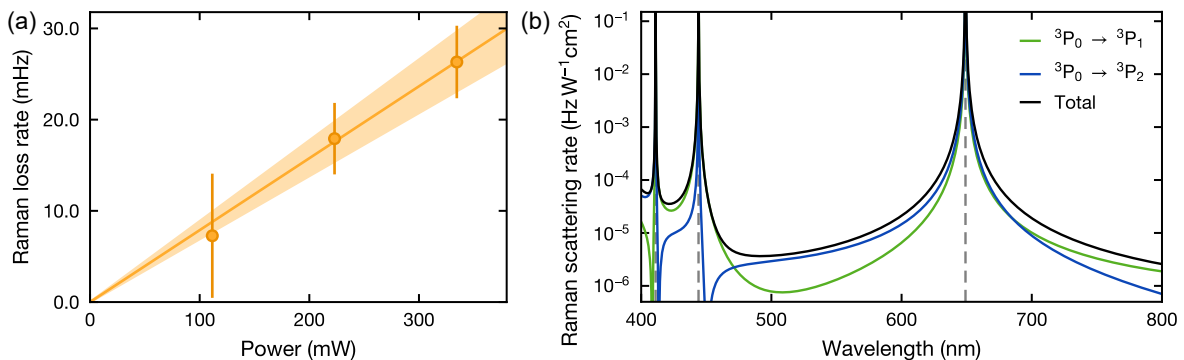


FIG. S3. **Raman loss rate at the tune-out wavelength and in the visible spectrum.** (a) The clock-state lifetime is reduced by the presence of the tune-out beam with a linear dependence of the Raman loss rate on the power. The error bars are obtained from the standard deviation of the individual lifetime fit uncertainties. The solid line is a weighted linear fit to the data, and the shaded area depicts the fit uncertainty. (b) Theoretical estimate of the intensity-dependent Raman scattering rate by generalizing the contributions of relevant transitions in Ref. [44].

latter is unknown (or undefined) for the contributions from “all other valence” as well as the core-excited contribution. But since these are high energy excitations, we approximate $\omega_{ki} \gg \omega, \omega'$ which means that these contributions are independent of wavelength. This assumption breaks down for short wavelengths, but since their relative contributions are small we nonetheless assume validity for wavelengths $\gtrsim 350$ nm. Finally, we note that while the results in Ref. [44] are listed for ${}^{171}\text{Yb}$, we perform our calculations for ${}^{174}\text{Yb}$. In doing so, we ignore any isotope effects to the reduced dipole matrix elements, i.e. intermediate state lifetimes. Isotope shifts to the fine-structure splittings ω_{if} and the excitation frequencies ω_{ki} are accounted for. Regardless, we estimate that isotope effects have negligible contribution. As a consistency check, we use the same approach to calculate the polarizability of ${}^3\text{P}_0$, $\alpha(\omega) = \alpha_i(\omega)$, for general frequencies ω . A comparison to our independent calculation described in Sec. S.II shows good agreement except very close to resonant transitions out of ${}^3\text{P}_0$, where details such as isotope shifts become more important. We believe this does not impact the calculations of the Raman scattering rates of interest.

Fig. S3(b) shows the Raman scattering rate for the two relevant two-photon transitions as a function of wavelength. As expected, divergences appear at resonances out of the ${}^3\text{P}_0$ state, whose locations are indicated by the dashed lines. The arrows indicate the two wavelengths of interest. At the 759 nm magic wavelength, our calculation reproduces the results of Ref. [44] (by construction, since no frequency conversion is needed here). There, the total scattering rate is $\Gamma_{{}^3\text{P}_0 \rightarrow {}^3\text{P}_1} + \Gamma_{{}^3\text{P}_0 \rightarrow {}^3\text{P}_2} = 4.40 \times 10^{-6} \text{ Hz}/(\text{W}/\text{cm}^2)$, with 65% of the scattering occurring to the ${}^3\text{P}_1$ state. At the tune-out wavelength, the total scattering rate is $10.2 \times 10^{-6} \text{ Hz}/(\text{W}/\text{cm}^2)$, which is the figure reported in the main text. We note that here the dominant scattering channel is reversed, with only 26% scattering to ${}^3\text{P}_1$.

S.VI. SYSTEMATIC UNCERTAINTIES IN THE MAGIC ANGLE MEASUREMENTS

Various error sources factor into the systematic uncertainty of the magic angle measurements, which we now discuss. Firstly we consider the uncertainty in the calibration between the current applied to bias coils and the resulting magnetic field. The bias coils consist of three separate coil pairs along x , y and z respectively. Each coil pair is calibrated via free-space spectroscopy of the ${}^3\text{P}_1$ Zeeman states, and results in relative uncertainties of 0.26% for the vertically oriented coils and 0.04% for the horizontal coils along y . Notably, by tracing the ${}^3\text{P}_1$ $m_J = 1$ resonance for various magnetic field angles we also find a small deviation from a perfectly orthogonal relative orientation between the fields created by these coils. The extracted angle of $90.9(2)^\circ$, referenced to the z coils, is compensated, but the uncertainty is included in the error budget. No magnetic field is created along x , though a small, ≈ 190 mG, uncompensated residual field along that direction contributes to the systematic uncertainty. Stray magnetic fields in the other directions are compensated to $\lesssim 10$ mG. The uncertainty in the lattice beam polarization is conservatively estimated by means of the transmission ratio of a polarizing beam splitter, resulting in a 0.07° contribution. However, this value also needs to include the relative angle between the normal vector to the breadboard and the z -direction of the coils, which mainly depends on the coil manufacturing and assembly process. We estimate 1 mm uncertainty in the lateral displacement between the z coil pair, resulting in a 0.92° uncertainty. This is the dominating factor of the total magnetic angle systematic error: combining the various independent uncertainties using the root sum square of the individual contributions, yields a total systematic uncertainty of 0.93° .

S.VII. SYSTEMATIC UNCERTAINTIES IN THE TUNE-OUT MEASUREMENT

Since saturation effects can play a significant role in the determination of tune-out wavelengths by means of parametric

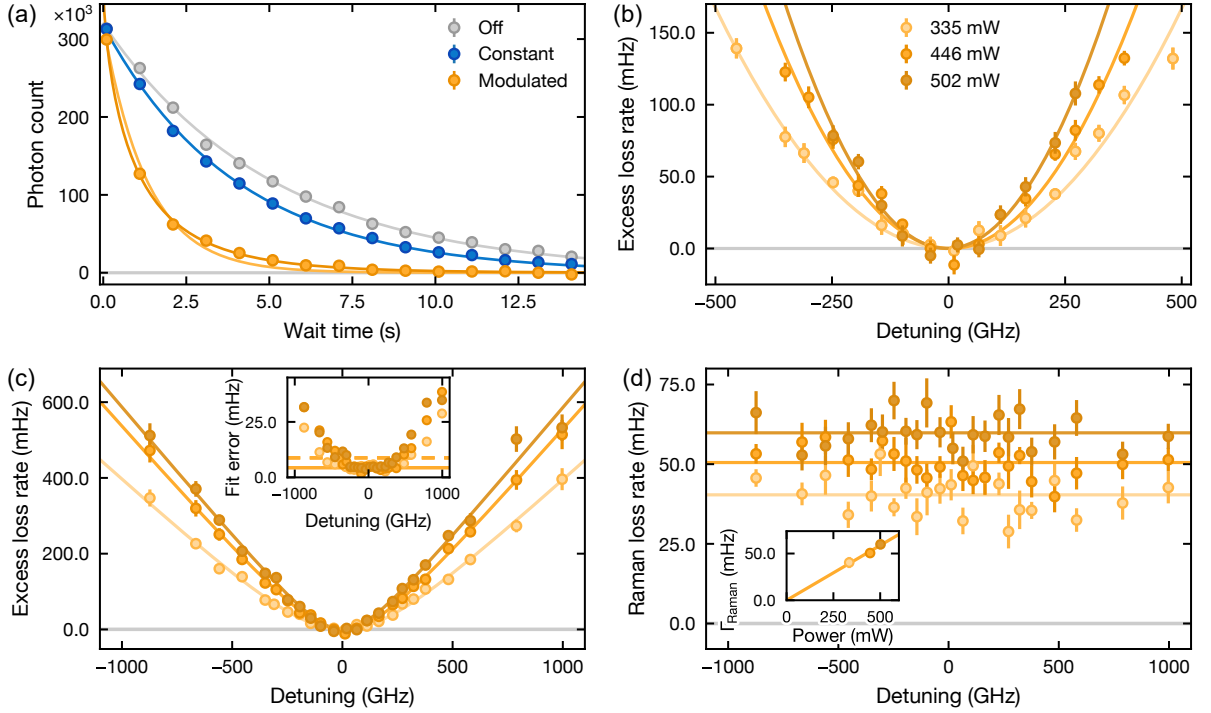


FIG. S4. **Assessing the systematic uncertainty from heating saturation effects and Raman losses.** (a) At large detunings and for a strong modulation, the total evolution of atom loss can no longer be described by a single exponential fit (light orange solid line). Instead, a super-exponential fit captures the time dynamics well (dark orange solid line). The loss rates without (gray) and an unmodulated (blue) tune-out lattice are not affected; the two solid lines show a single exponential fit. (b) Restricted data set based on the fit uncertainty as described in the text and displayed in (c) as an inset, to limit saturation effects. The data is fitted with a quadratic fit function without offset (solid lines). The data at a tune-out power of 446 mW is shown in the main text. (c) Complete dataset, which shows a linear evolution for large detunings, necessitating fits with the empirical function (S.7) to obtain bounds on the systematic error. Inset: The single exponential fit uncertainty propagated from the modulated and unmodulated lifetime fits remains approximately constant for small detunings and rapidly diverges once the saturation effect starts to become relevant. We define the acceptance threshold (dashed line) to be twice the mean fit uncertainty for small detunings (solid line). (d) Upon comparing the lifetime in the presence of a constant tune-out beam and the one without, we do not observe any significant trends as a function of laser detuning. The solid lines represent the means of the Raman loss rates for each power level (color coded as in the other subfigures and the inset). Inset: The dependence of the mean Raman loss rate on the power is linear, in agreement with Fig. S3(a).

heating schemes [26], we perform three lifetime measurements with varying modulation powers at each selected tune-out laser frequency. This results in varying detuning ranges, at which the saturation effect starts to become relevant. We determine this onset using the exponential fit uncertainty of the modulated lifetime curves, which starts to increase beyond the base value of $\sigma \simeq 4$ mHz due to deviations from a single exponential decay [Fig. S4(a)]. We attribute this to be the result of spatial inhomogeneities in the parametric heating due to the incommensurability of the lattices, combined with strongly varying tunneling rates depending on the harmonic oscillator state an atom occupies. For a strong modulation, where the perturbative approach fails, this leads to rapid loss of initially relatively hot atoms independent of their initial position, while the coldest atoms can remain cold for comparably long times if they reside on lattice sites that do not observe strong effective amplitude modulation. The resulting loss trend can be approximated by a super-exponential function $N_0 e^{-(\Gamma t)^\alpha}$, which indeed captures the data well. For the tune-out value mentioned in the main text we select an upper bound of the fit uncertainty of $2\sigma = 8.8$ mHz, beyond which all datapoints are

excluded. Since we moreover select symmetrically spaced detunings around the tune-out wavelength, which are additionally chosen to be equidistant close to f_{to} , we choose a symmetrically truncated dataset to prevent bias. This leads to a dataset that contains 17 distinct wavelengths for the lowest optical power of $\simeq 335$ mW, 15 for 446 mW, and 11 for 502 mW [Fig. S4(b)]. For these subsets, we find the expected simple quadratic fit without offset to describe the data well, as confirmed with a χ^2 test. For an in-depth discussion of the perturbative derivation of this functional dependence we refer to Refs. [29, 52]. To obtain an estimate of the systematic uncertainty due to undetected and uncorrected heating saturation, we additionally perform a fit to these subsets as well as to the complete datasets with the function

$$\Gamma_{\text{exc}}(\Delta) = A \left(\sqrt{B\Delta^2 + 1} - 1 \right), \quad (\text{S.7})$$

where A and B are the fitting parameters, that describes a quadratic function for small detunings and becomes linear for large Δ . This empirical function takes the deviation from the perturbative quadratic scaling result due to the emergence of

an additional loss timescale into account. The extremal discrepancies from f_{t_0} amount to +5.7 GHz and -4.5 GHz for the full and restricted dataset, respectively, and we conservatively assume these values to quantify the systematic uncertainty to the tune-out measurement.

We exclude other sources of potential systematic uncertainties, such as different mean intensity levels for the modulated and the constant case, by analyzing sample photodiode traces. While we notice a slightly larger mean photodiode voltage upon modulation, this effect only amounts to a relative dif-

ference of 0.4(9)%, i.e., within the measurement uncertainty, and corresponds to an enhanced Raman loss rate of 0.2(5) mHz for the dataset at 502 mW. The inclusion of a corresponding offset into the fit function further does not affect the results noticeably and is therefore not applied for the values reported in the main text. Moreover, the computed Raman loss rate only varies by 5% over the whole detuning range of 1.9 THz, allowing us to treat it as approximately constant. Likewise, the deviation of the calculated polarizability curve from a linear function due to its curvature amounts to less than 1% and is therefore neglected.